Chinese Chemical Letters 37 (2026) 110728

Contents lists available at ScienceDirect

Chinese Chemical Letters

journal homepage: www.elsevier.com/locate/cclet

Superior comprehensive performance in sodium niobate-based high-entropy relaxors

Kun Wei[a], Jianhong Duan[a], Linzhao Ma[a], Qianbiao Du[a], Huifen Yu[b], Xuefan Zhou[c], Hao Li[a,*], He Qi[b,*], Dou Zhang[c,*]

[a] College of Electrical and Information Engineering, Hunan University, Changsha 410082, China
[b] Beijing Advanced Innovation Center for Materials Genome Engineering Department of Physical Chemistry, University of Science and Technology Beijing, Beijing 100083, China
[c] Powder Metallurgy Research Institute, State Key Laboratory of Powder Metallurgy, Central South University, Changsha 410083, China

ARTICLE INFO

Article history:
Received 7 November 2024
Revised 5 December 2024
Accepted 5 December 2024
Available online 6 December 2024

Keywords:
Sodium niobate
Pb-free
Ergodic relaxor state
Oxygen octahedral tilt
Energy storage performance

ABSTRACT

Cutting-edge high/pulsed power capacitors with satisfactory power density are fundamental units in modern power storage systems. However, a persistent challenge is how to overcome the trade-off between recoverable energy storage density (W_{rec}) and efficiency (η) for meeting the miniaturization and integration of advanced applications. Here, multiple local distortions including inhomogeneous functional nanoclusters, (anti)ferro-distortions and highly dynamic polar nanoregions are modulated through a high-entropy strategy to design a stable ergodic-relaxor-state-dominated structure. Of great importance, this strategy delay polarization saturation, reduces hysteresis and improves breakdown strength, so that an ultrahigh W_{rec} ~11.94 J/cm^3 with a $\eta \sim 82.4\%$ is realized in Pb-free ergodic-relaxors. Moreover, a significant Vickers hardness of 10.04 GPa as well as superior temperature, cycling and frequency stabilities are also obtained. This work demonstrates that designing multiple local distortions *via* a high-entropy strategy is a promising way to realize superior comprehensive energy storage properties in high/pulsed power capacitors.

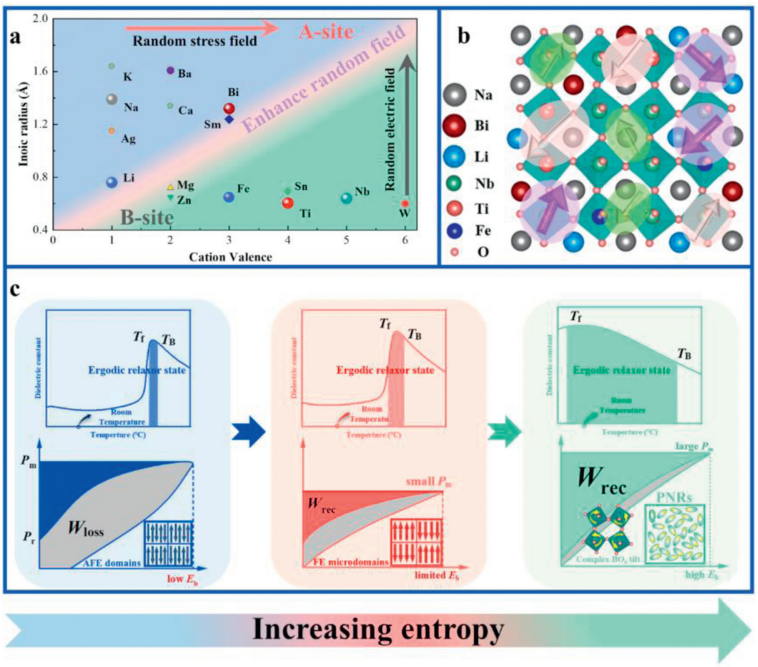
© 2025 Published by Elsevier B.V. on behalf of Chinese Chemical Society and Institute of Materia Medica, Chinese Academy of Medical Sciences.

The proposal of "carbon neutrality" challenges the development of renewable energy and dependable storage solutions [1]. Dielectric capacitors are vital for contemporary energy systems, providing a higher power density and a faster-discharging rate compared to other energy storage systems across various applications, from portable electronics to electric vehicles and grid storage [2–10]. However, the application of dielectric capacitors is seriously restricted by their limited energy storage density and poor reliability in harsh environments, particularly in metallurgical monitoring, avionics and mining [11,12]. Accordingly, there is a center of concern toward the exploitation of dielectric capacitors with high energy storage density and high reliability.

In terms of energy storage properties (ESPs), the integration of large and delayed saturation polarization (P_m), small remanent polarization (P_r), low hysteresis (H), as well as a high breakdown strength (E_B) is essential to achieving high recoverable storage density (W_{rec}) and conversion efficiency (η) [13–15]. Advances in materials science, particularly in Pb-free ceramics, have significantly enhanced ESPs. For example, the polarization features are modulated by means of phase structure [16], domain size [17], relaxation enhancement [18], etc. to reduce the P_r and H, which can significantly enhance η. The other hand, preparation process optimization like viscous polymer processing (VPP) [19], hot-pressing [20] and repeated rolling [21], high energy ball milling [22] as well as chemical modifications, such as defect engineering [23] and interfacial polarization [24], can effectively enhance E_B. Besides, special structures such as "core–shell structure" [25,26], "local polymorphic distortion" [27] and "element segregation" [28] are also used to improve ESPs. These strategies offer superior energy storage capabilities, which is essential for next-generation dielectric capacitors. Recently, significant breakthroughs in the W_{rec} of relaxor ferroelectrics (RFEs) and antiferroelectrics (AFEs) have distinguished them from other types of Pb-free ceramics. Extremely high W_{rec} of 7.9 [29] and 12.2 J/cm^3 [19] in $AgNbO_3$ (AN), $NaNbO_3$ (NN)-based AFE systems have been achieved. Unfortunately, unsatisfactory η (<80%) causes the energy loss (W_{loss}) to escape in the form of heat, which leads to thermal breakdown of the capacitor after multiple runs [30]. For RFEs, the progressive transition from nonergodic to ergodic relaxor (ER) state on heating leads to a monoton-

* Corresponding authors.
E-mail addresses: hli@hnu.edu.cn (H. Li), qiheustb@ustb.edu.cn (H. Qi), dzhang@csu.edu.cn (D. Zhang).

https://doi.org/10.1016/j.cclet.2024.110728
1001-8417/© 2025 Published by Elsevier B.V. on behalf of Chinese Chemical Society and Institute of Materia Medica, Chinese Academy of Medical Sciences.



Scheme 1. (a–c) Schematic of designing multiple local distortion *via* a high-entropy strategy in ergodic relaxors for high energy storage.

ically lower H, improving η [31]. However, most RFEs still exhibit confined W_{rec} (<8 J/cm^3) as the interactions between polar nanoregions (PNRs) are weakened, resulting in a low P_m [26]. Therefore, achieving both high W_{rec} (>10 J/cm^3) and high η (>80 %) in bulk ceramics remains a challenge to be addressed urgently.

NN with multi-phase exhibits high adjustability in the ordering of both polarization and oxygen octahedral tilt, making it an outstanding matrix for local structure design [32,33]. Over 10 types of structures have been reported regarding NN-based systems, but only a limited number of NN-based systems with ER state (NN–CZ, NN-BMN-BNST, NN-BF-BT, *etc.*) have been reported [28,34,35]. Here, $(Na_{0.9-x}Bi_{0.1+x/2}Li_{x/2})(Nb_{0.9-x}Fe_{0.1}Ti_x)O_3$ (NBLNFT-x) ERs with multiple local distortions are devised through a simple high-entropy strategy, as shown in Scheme 1. The configuration entropy (S_{config}) of NBLNFT-x is listed in Table S1. Bi^{3+} with the "lone pair effect" and the large center-off displacement value results from Li^+ with a small ionic would effectively enhance polarization saturation [35]. Fe^{3+} and Ti^{4+} have similar ionic radii and theoretical polar displacement values compared to Nb^{5+}, which can be considered as the ferroelectrically active ion, are usually accompanied by large P_m [36]. Besides, the introduction of these ions (Li^+, Bi^{3+}, Fe^{3+}, Ti^{4+}) into NN matrix simultaneously enhances the local random electric field and stress field (Scheme 1a). This phenomenon facilitates the formation of highly dynamic PNRs, which would significantly lower the domain-switching energy barrier and promote polarization rotation [37]. With increasing S_{config}, the mismatch in atomic size, mass, valence, and electronegativity is amplified, which not only enables a broader temperature range for the ER state but also induces disordered polarization configuration (Scheme 1b), thus significantly enhance the response to external electric field, greatly enhance η (Scheme 1c) [38,39]. Moreover, complex (anti)ferro-distortions including local ordered and disordered domain structures result from long-range ordered and disordered oxygen octahedral tilts, respectively, which would provide large and delayed saturation polarization [40,41]. As a result, encouraging high-field ESPs (W_{rec} ~ 11.94 J/cm^3, η ~ 82.4 % at 66 kV/mm) and temperature stability at 40 kV/mm (W_{rec} ~ 5.0 ± 0.3 J/cm^3, η ~ 80.69 % ± 4 %, from 25 °C to 150 °C) are realized in NBLNFT-0.3 ceramic. Furthermore, an ultra-high Vickers hardness H_v ~ 10.03 Gpa is also obtained owing to the combination of the dense microstructure and fine grain size [42]. The superior comprehensive performance enable NN-based an attractive research topic in Pb-free dielectric ceramic field.

The systems of NBLNFT-x were achieved through a solid-state sintering method. Details of equations, preparation process, structural characterization, phase field simulation and measurement equipment are presented in Supporting Information.

Mechanical properties like hardness are critical parameters that affect the cyclic life of the material. Figs. 1a and b present symmetrical rhombic Vickers diamond indentations and diagonal straight cracks indicating plastic deformation of the ceramic. A significant enhancement in H_v ~ 10.04 Gpa is gained in NBLNFT-0.3 ceramic compared to NBLNFT-0 ceramic (6.63 Gpa) with the increase in S_{config}. In comparison to glass and other perovskite systems, the NBLNFT-0.3 ceramic shows higher hardness, as plotted in Fig. 1c [42–49]. Powder XRD patterns of NBLNFT-x (Fig. 1d) ceramics exhibit a perovskite structure without impurity phases. The (200) peak displacing to higher angles is caused by lattice contraction resulting from the solid solution of components with smaller ionic radii (Fig. 1e). In addition, the split (200) peaks in NBLNFT-0 ceramic progressively merge as x increases, which is similar to the formation of pseudo-cubic phases in typical relaxors [50]. Rietveld refinements for XRD the pattern of NBLNFT-x ceramics using Fullprof software are shown in Fig. 1f and Fig. S1 and Table S2 (Supporting information). It is interesting that a transformation from AFE P phase to FE Q phase is found in $0 \le x \le 0.2$ ceramics, and the NBLNFT-0.3 ceramic can be well identified by FE Q phase, indicating the intrinsic properties of NBLNFT-x have changed from AFE to RFE with the increased entropy. The dielectric spectra, plotted in Fig. 1g and Fig. S2 (Supporting information), also demonstrate the disappearance of antiferroelectricity and the formation of relaxor ferroelectricity in NBLNFT-x ceramics [51]. Furthermore, the relaxation degree (γ) of NBLNFT-0.3 ceramic calculated by the Curie–Weiss law is 1.89, suggesting a strong relaxor behavior. The Raman spectra of $x \ge 0.2$ ceramics (Fig. 1h and Fig. S3 in Supporting information) similarly demonstrates localized relaxor ferroelectric behavior [52]. Measurement of the unipolar P-E loops at 15 kV/mm is utilized for the initial assessment of ESPs in NBLNFT-x ceramics

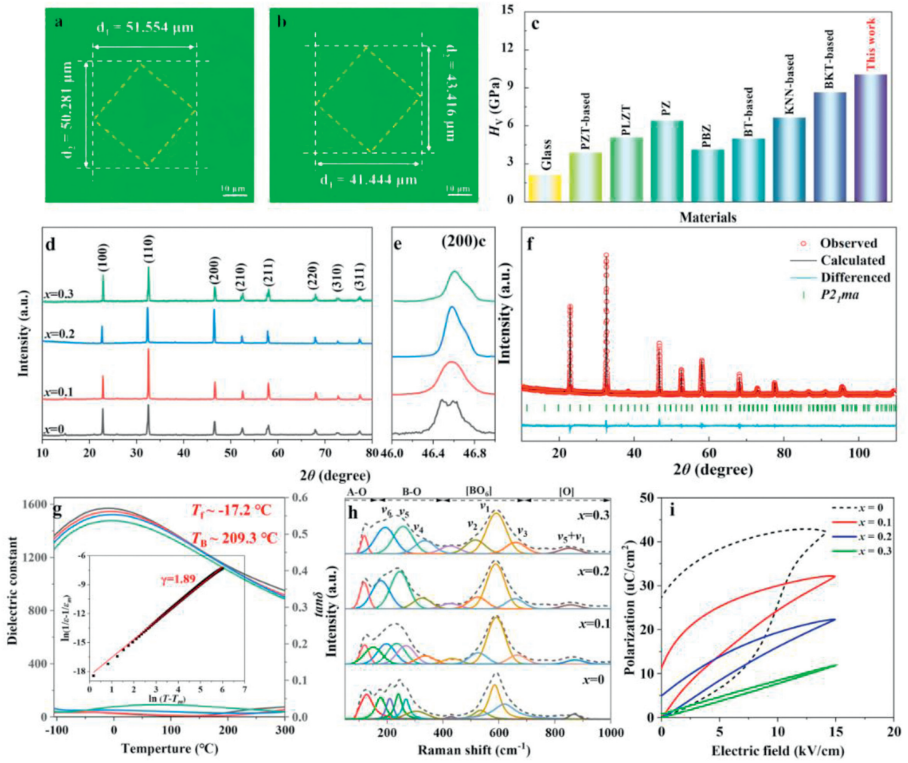


Fig. 1. Vickers indentation of (a) NBLNFT-0, (b) NBLNFT-0.3 ceramics, (c) Vickers hardness of recently reported glass and ceramic materials. (d) XRD patterns of NBLNFT-*x* ceramics. (e) Enlarged view of the 2θ range from 46° to 47° (f) XRD Rietveld refinement of NBLNFT-0.3 ceramic. (g) Dielectric spectra of NBLNFT-0.3 ceramic. (h) Raman spectra of NBLNFT-*x* ceramics. (i) *P*-*E* loops of NBLNFT-*x* ceramics under 15 kV/mm.

(Fig. 1i). The ceramic of NBLNFT-0 presents a classic AFE feature with a high P_m but a large P_r. With increasing S_{config}, P_m, H and P_r exhibit an ongoing trend of decreasing, especially in NBLNFT-0.3 ceramic, where an exceedingly slim *P*-*E* loop is obtained. This phenomenon is associated with the transition of NBLNFT-*x* from AFE to RFE, which is in accordance with the results of both the dielectric spectrum and XRD. On account of the ESPs in the low-*E* region, the NBLNFT-0.3 high-entropy ceramic with an ER state is considered to be the optimal component to realize both high W_{rec} and η, thus further investigations on its microstructure are carried out.

For the identification of the local polar structure, TEM analysis of the NBLNFT-0.3 ceramic along the $[100]_c$ and $[011]_c$ directions are presented in Figs. 2a–j. An anomalous microdomain with sub-micrometer-grade widths and micron-grade lengths, associating with long-range ordered oxygen octahedral tilt in the NN matrix [53], which would result in high P_{max} (Fig. 2a). Fig. 2b presents the HR-TEM lattice fringe, demonstrating good crystallinity. As a symbol of RFEs, PNRs with lower domain-switching energy barriers and weaker coupling, which can significantly reduce *H* and delay polarization saturation, should not be ignored [3,4,54,55]. A complex domain pattern composed of randomly dispersed PNRs with sizes of 2–5 nm (Fig. 2d) can be observed on the HR-TEM image, and the corresponding inverse Fourier transform pattern (Fig. 2e) along the $[100]_c$ direction both indicate the disordered polarization configuration. It is usually thought that ferroelastic domain is generally assumed to be formed through the (anti)ferrodistortion of both polarization and oxygen octahedral tilt. Therefore, the anomalous microdomain in Fig. 2a can be defined as the micro-ferroelastic domain, in which the PNRs are distributed disorderly. Simultaneously, the 1/2-type superlattice diffraction dots like (*ooe*)/2 are observed (Fig. 2c), which originate from the tilting of the $a^-b^+c^-$ oxygen octahedral in the FE Q phase [34]. Notably, 1/2-type superlattice diffraction dots disappear at partial equivalent positions. It is because that the micro-ferro-elastic domains arising from the long-range ordered oxygen octahedral tilt leads to partial occupation of the superlattice diffraction dots. The local polar structure observed along $[100]_c$ direction in NBLNFT-0.3 is similar to the typical NN–CZ RFEs with long-range ordered oxygen octahedral tilt and disordered polarization [34]. Apart from the anomalous microdomains, numerous black speckled nanoclusters can be observed on the TEM image along the $[011]_c$ direction (Fig. 2h). In an attempt to explore the origin of the black speckles, a yellow selected region is magnified. A particular type of inhomogeneous lattice stripe (20–50 nm) is discovered (Fig. 2i), which results in the appearance of different contrasts (black speckles), also indicating the disordered polarization configuration. The 1/2-type superlattice diffraction dots like (*eeo*)/2 and (*ooo*)/2 that can be viewed at all equivalent positions, demonstrating the absence of local ordered oxygen octahedral tilt. Therefore, the NBLNFT-0.3 ceramic can be considered as an RFE, in which nanoregions with inhomogeneous polarization vectors are randomly embedded in ordered micro-ferroelastic domains and disordered nanoclusters. The simultaneous existence of long-range ordered and disordered oxygen octahedral tilt provides the NBLNFT-0.3 ceramic with a large polarization response and delayed polarization saturation, while disordered polarization configuration weakens the domain-switching barriers, leading to flatter switching pathways and smaller hysteresis losses, thus extremely boosting the energy density. Moreover, PFM is employed to recognize the response of PNRs to *E* (Figs. 2k and l). It is clearly shown that the PFM images of the NBLNFT-0 ceramic under ±30 V exhibit large domain switching. There is still a large domain signal after 20 min of relaxation with the removal of *E*, which is consistent with a large *H* in the *P*-*E* loop [56]. On the contrary, the domain signal of NBLNFT-0.3 ceramic after 20 min of relaxation is rapidly switched over to the initial state, suggesting the existence of high dynamic PNRs. These observations provide concrete evidence for establishing multiple local distortions including inhomogeneous functional nanoclusters, (anti)ferro-distortion and

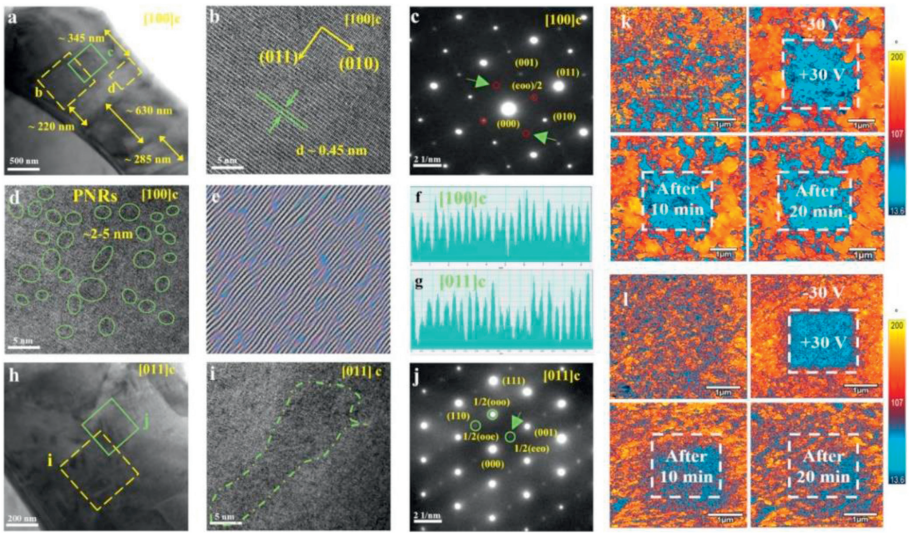


Fig. 2. Domain structure of NBLNFT-0.3 ceramic. Bright-field TEM images and the corresponding SAED patterns along (a–f) the $[100]_c$ and (g–j) $[011]_c$ directions. Out-of-plane PFM phase images of (k) NBLNFT-0 and (l) NBLNFT-0.3 ceramics.

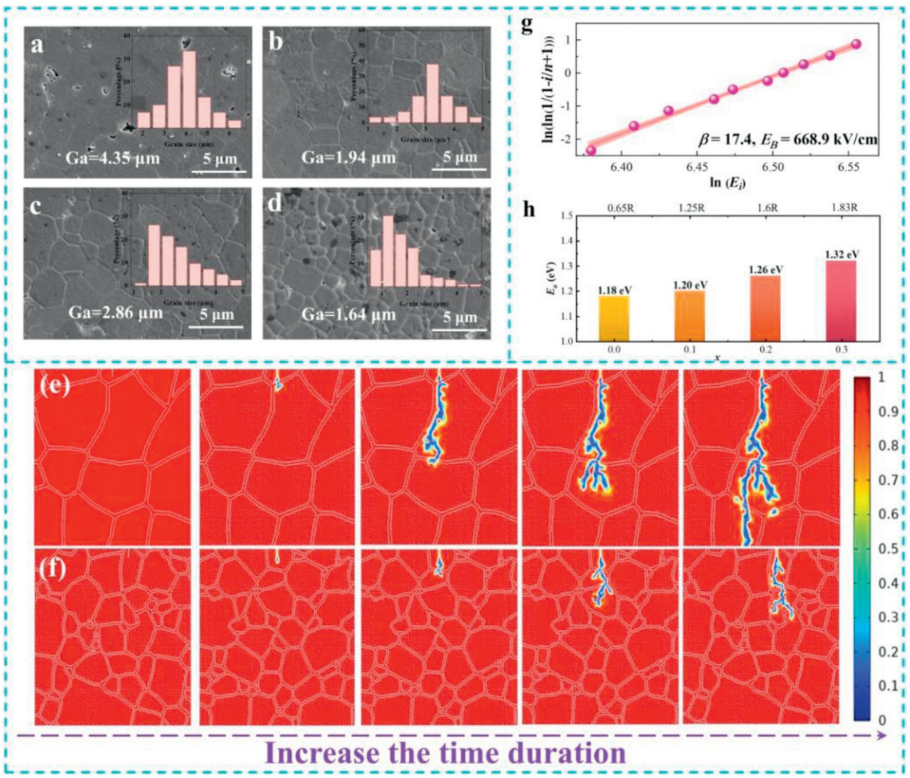


Fig. 3. (a–d) SEM images of NBLNFT-*x* ceramics. Electrical tree evolution for (e) NBLNFT-0, (f) NBLNFT-0.3 ceramics. (g) Weibull distributions of NBLNFT-0.3 ceramic. (h) The E_a values of NBLNFT-*x* ceramics.

highly dynamic polar nanoregions through a high-entropy strategy, which is significant for improving the energy storage capacity of NBLNFT-0.3 ceramic.

In accordance with the theory of energy storage, outstanding E_B is also crucial for gaining a high W_{rec}. It is widely recognized that the smaller average grain size (AGS) represents the larger E_B, denoted as $E_B \propto (AGS)^{-\alpha}$ ($\alpha \sim 0.2$–0.5) [57,58]. Figs. 3a–d present the SEM images and the AGS of NBLNFT-*x* ceramics. Inhomogeneous morphology with many pores and large AGS (4.35 μm) can be viewed in NBLNFT-0, which is responsible for the low E_B. With increasing *x*, the pores disappear and the morphology gradually becomes denser. More importantly, AGS declines sharply, even 1.64 μm of that is realized in NBLNFT-0.3 ceramic. The uniform distribution of the elements in NBLNFT-0.3 ceramic is shown in the EDS mapping (Fig. S4 in Supporting information). Simulation using the finite element method, combined with surface morphology and the dielectric constant, is employed to deeply understand the impact of microstructure on the breakdown process. Figs. 3e and f and Fig. S5 (Supporting information) present the electrical tree propagation as well as the distribution of potential and local *E*-field. The NBLNFT-0 suffers from a sizable local *E*-field and a remarkable electric potential difference under the external *E*, so that the electrical tree grows rapidly with time and eventually punctures the whole model. In contrast, the decreased AGS and the increased

grain boundaries in NBLNFT-0.3 ceramic lead to a smoother grain-to-boundary transition with a homogeneous distribution of local *E*-field and potential difference, inhibiting the rapid growth of electrical tree. The Weibull distribution used to assess the statistical E_B value is depicted in Fig. 3g, and both the well-fitted distribution and a high shape parameter ($\beta = 17.4$) demonstrate high reliability [59]. Besides, the Nyquist patterns of NBLNFT-*x*, measured between 500 °C and 650 °C, are plotted in Fig. S6. The dramatic increased resistance with increasing S_{config} suggests an enhancement in electrical insulation. The activation energy (E_a) calculated *via* the Arrhenius formula is shown in Fig. 3h. Inhibition of carriers across grain boundaries by the highest E_a (1.32 eV) in NBLNFT-0.3 ceramic also improves the insulating property effectively [3,60]. Overall, these improvements ensure an ultrahigh E_B can be realized in NBLNFT-0.3 high-entropy ceramic.

Based on the devise of multiple local distortions through a high-entropy strategy, an encouraging energy storage capability is achieved in NBLNFT-0.3 high-entropy ceramics with thicknesses of 0.05–0.08 mm (Fig. 4). As displayed in Fig. 4a, the attainment of slender *P-E* loops with small P_r even at high *E* demonstrates a stable polarization behavior. Remarkably, a high $P_{max} \sim 47.04$ μC/cm^2 together with a low $P_r \sim 2.8$ μC/cm^2 at 66 kV/mm is gained. This means an exciting $W_{rec} \sim 11.9$ J/cm^3 accompanied by a high $\eta \sim 82.4$% has been realized (Fig. 4b). The outstanding ESPs obtained in NBLNFT-0.3 high-entropy ceramic are still a huge breakthrough compared to other ceramics reported so far (Fig. 4c and Table S3 in Supporting information). Importantly, there is no indication of polarization saturation even at E_B, meaning NBLNFT-0.3 has the potential to be the energy storage material used in MLCC with thinner thicknesses for achieving higher performance [61]. High reliability is an essential index for assessing the outdoor operation of capacitors. Figs. 4d–f present the temperature/cycling/frequency-dependent *P-E* loops and the corresponding ESPs of NBLNFT-0.3 ceramic under 40 kV/mm. The *P-E* loops are always very thin, with near-zero changes in P_{max} as the temperature rises from 25 °C to 150 °C. Consequently, the high W_{rec} (5.0 ± 0.3 J/cm^3) and η (80.69% ± 5%) over the temperature range can be sustained. Such excellent temperature insensitivity is strongly associated with virtually unchanged phase structure [62], which can be proved by in-situ Raman spectrum (Fig. S7 in Supporting information). Moreover, the *P-E* loops also remain thin over a long cyclic behavior (1–10^5) and a wide frequency (1–500 Hz). As a result, durable cycling performance ($W_{rec} \sim 5.19 \pm 0.31$ J/cm^3, $\eta \sim 81.8\% \pm 2.26\%$) and stable frequency conversion performance ($W_{rec} \sim 4.96 \pm 0.32$ J/cm^3, $\eta \sim 82.51\% \pm 1.53\%$) can be achieved. Such superior reliability ensures that NBLNFT-0.3 high-entropy ceramics have a promising prospect in practical application environments. The charge/discharge performance is also significant for a comprehensive assessment of the potential for capacitor applications [63,64]. Viewed from the regular overdamped discharge oscillating waveforms under *E* from 10 kV/mm to 35 kV/mm (Fig. 4g), the peak current (I_{max}) progressively rises from 3.38 A to 11.85 A. Accompanying the growth of I_{max} is a simultaneous increase in W_{dis}, which reaches a maximum valve (3.24 J/cm^3 at 35 kV/mm). It is worth noting that an ultrafast discharge rate ($t_{0.9} \sim 44$ ns) can be acquired at each selected *E* (Fig. 4h). Apart from the overdamped discharge, the underdamped discharge process, plotted in Fig. S8 (Supporting information), also shows an excellent performance. The I_{max}, the current density (C_D) as well as the power density (P_D) reach as high as ~24.6 A, ~783.6 A/cm^2 and ~137.1 MW/cm^3, respectively, under 35 kV/mm. A comparison of comprehensive electrical properties between NBLNFT-0.3 and other representative systems (NN, BNT, AN, BF, BT, ST) of Pb-free bulk energy storage ceramics is given in Fig. 4i. Obviously, NBLNFT-0.3 ceramic possesses significant advan-

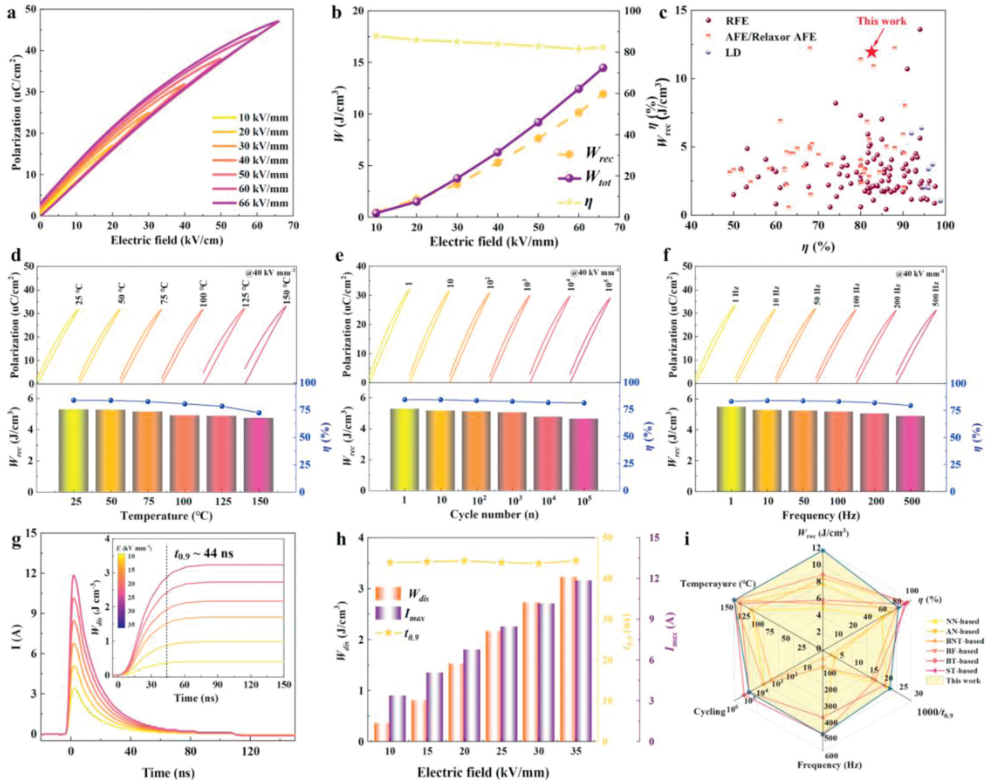


Fig. 4. Energy storage performance of NBLNFT-0.3 ceramic. (a) Electric field-induced unipolar polarization loops, (b) Calculated W_{tot}, W_{rec} and η. (c) Comparison of the W_{rec} and η with these reported Pb-free bulk ceramics. (d) Temperature-dependent, (e) cycling-dependent, (f) frequency-dependent. (g) Overdamped pulsed discharge current curves and W_{dis}-$t_{0.9}$ plots (inset) under different electric fields. (h) W_{dis}, I_{max} and $t_{0.9}$ as a function of electric field. (i) Comparisons of comprehensive properties between NBLNFT-0.3 ceramic and some representative energy storage ceramics with excellent comprehensive performance of different systems.

tages in terms of ESPs, reliability and discharge performance, particularly in high temperature/cycling/frequency conditions. In view of these, the more significant advantage in comprehensive ESPs than other systems exhibited by NBLNFT-0.3 high-entropy ceramic makes for a promising future in dielectric capacitors [29,60,65–68].

In summary, outstanding ESPs along with excellent reliability and high H_v is realized in NBLNFT-0.3 ceramic. Multiple local distortions including inhomogeneous functional nanoclusters, complex local (anti)ferro-distortions and highly dynamic polar nanoregions are modulated through the regulation the configurational entropy. These local distortions effectively prevent early polarization saturation, minimize hysteresis loss, decrease P_r and improve mechanical properties. Encouraging high-field ESPs ($W_{rec} \sim 11.94\,J/cm^3$, $\eta \sim 82.4\%$ at 66 kV/mm) and temperature stability at 40 kV/mm ($W_{rec} \sim 5.0 \pm 0.3\,J/cm^3$, $\eta \sim 80.69\% \pm 5\%$, from 25 °C to 150 °C) are realized. All results demonstrate that designing multiple local distortion through a high-entropy strategy offers new ways to realize superior comprehensive properties.

Declaration of competing interest

The authors declare that they have no known competing financial interests or personal relationships that could have appeared to influence the work reported in this paper.

CRediT authorship contribution statement

Kun Wei: Writing – original draft, Visualization, Validation, Investigation, Formal analysis, Data curation, Conceptualization. **Jianhong Duan:** Writing – review & editing, Visualization. **Linzhao Ma:** Writing – review & editing, Visualization. **Qianbiao Du:** Writing – review & editing, Visualization. **Huifen Yu:** Writing – review & editing, Visualization. **Xuefan Zhou:** Writing – review & editing, Visualization. **Hao Li:** Writing – review & editing, Software, Resources, Project administration, Funding acquisition. **He Qi:** Writing – review & editing, Supervision. **Dou Zhang:** Writing – review & editing, Supervision.

Acknowledgments

This work was supported by the National Natural Science Foundation of China (No. 52102129), the Hunan Provincial Natural Science Foundation of China (No. 2023JJ30138), the Science Technology Innovation Program of Hunan Province (No. 2023RC3094) and the State Key Laboratory of Powder Metallurgy, Central South University, Changsha, China.

Supplementary materials

Supplementary material associated with this article can be found, in the online version, at doi:10.1016/j.cclet.2024.110728.

References

[1] M. Feng, Y. Feng, T. Zhang, et al., Adv. Sci. 8 (2021) e2102221.
[2] H. Pan, S. Lan, S. Xu, et al., Science 374 (2021) 100–104.
[3] M. Zhang, S. Lan, B. Yang, et al., Science 384 (2024) 185–189.
[4] H. Pan, F. Li, Y. Liu, et al., Science 365 (2019) 578–582.
[5] G. Wang, Z. Lu, Y. Li, et al., Chem. Rev. 121 (2021) 6124–6172.
[6] Z. Chen, H. Lin, Y. Tan, et al., Adv. Funct. Mater. 34 (2024) 2407653.
[7] X. Liu, Z. Sun, Y. Sun, et al., Adv. Funct. Mater. 33 (2023) 2307205.
[8] Y. Tong, Y. Wu, Z. Liu, et al., Chin. Chem Lett. 34 (2023) 107443.
[9] Z. Chen, Y. Wu, X. Liu, Y. Zhang, et al., J. Energy. Chem. 81 (2023) 462–471.
[10] Y. Tan, H. Lin, Z. Chen, et al., J. Energy. Chem. 99 (2024) 365–374.
[11] H. Qi, R. Zuo, A. Xie, et al., Adv. Funct. Mater. 29 (2019) 1903877.
[12] H. Qi, R. Zuo, J. Mater. Chem. A 7 (2019) 3971–3978.
[13] S. Wang, F. Yan, J. Qian, et al., Energy Storage Mater. 66 (2024) 103155.
[14] B. Yang, Y. Zhang, H. Pan, et al., Nat. Mater. 21 (2022) 1074–1080.
[15] S. Wu, B. Fu, J. Zhang, et al., Small 19 (2023) e2303915.
[16] S. Li, T. Hu, H. Nie, et al., Energy Storage Mater. 34 (2021) 417–426.
[17] K. Wei, J. Duan, X. Zhou, et al., ACS Appl. Mater. Interfaces 15 (2023) 48354–48364.
[18] N. Luo, K. Han, M.J. Cabral, et al., Nat. Commun. 11 (2020) 4824.
[19] X. Wang, X. Wang, Y. Huan, et al., ACS Appl. Mater. Interfaces 14 (2022) 9330–9339.
[20] F. Li, X. Hou, T. Li, et al., J. Mater. Chem. C 7 (2019) 12127–12138.
[21] B. Guo, Y. Yan, M. Tang, et al., Chem. Eng. J. 420 (2021) 130475.
[22] L. Chen, T. Hu, X. Shi, et al., Adv. Mater. 36 (2024) e2313285.
[23] H. Wang, E. Li, K. Wei, et al., ACS Appl. Mater. Interfaces 14 (2022) 54021–54033.
[24] W. Cao, R. Lin, X. Hou, et al., Adv. Funct. Mater. 33 (2023) 2301027.
[25] X. Dong, X. Li, X. Chen, et al., Nano Energy 101 (2022) 107577.
[26] S. Xie, Y. Chen, Q. He, et al., Chin. Chem Lett. 35 (2024) 108871.
[27] L. Chen, S. Deng, H. Liu, et al., Nat. Commun. 13 (2022) 3089.
[28] X. Zhou, G. Xue, Y. Su, et al., Chem. Eng. J. 458 (2023) 141449.
[29] H. Yuan, X. Fan, Z. Zheng, et al., Chem. Eng. J. 456 (2023) 141023.
[30] Z. Lv, T. Lu, Z. Liu, et al., Adv. Energy Mater. 14 (2024) 2304291.
[31] L. Chen, N. Wang, Z. Zhang, et al., Adv. Mater. 34 (2022) 2205787.
[32] H. Qi, G. Wang, Y. Zhang, et al., Acta Mater. 248 (2023) 118778.
[33] S.K. Mishra, N. Choudhury, S.L. Chaplot, et al., Phys. Rev. B 76 (2007) 024110.
[34] H. Qi, W. Li, L. Wang, et al., Mater. Today 60 (2022) 91–97.
[35] A. Xie, R. Zuo, Z. Qiao, et al., Adv. Energy Mater. 11 (2021) 2101378.
[36] H. Liu, Z. Sun, J. Zhang, H. Luo, et al., J. Am. Chem. Soc. 146 (2024) 3498–3507.
[37] C. Long, Z. Su, H. Song, et al., Energy Storage Mater. 65 (2024) 103055.
[38] R. Kang, Z. Wang, W. Yang, et al., J. Mater. Chem. A 9 (2021) 24387–24396.
[39] W. Yang, H. Zeng, F. Yan, et al., J. Mater. Chem. A 10 (2022) 11613–11624.
[40] H. Liu, Z. Sun, J. Zhang, et al., J. Am. Chem. Soc. 145 (2023) 19396–19404.
[41] H. Liu, Z. Sun, J. Zhang, et al., J. Am. Chem. Soc. 145 (2023) 11764–11772.
[42] L. Chen, F. Long, H. Qi, et al., Adv. Funct. Mater. 32 (2022) 2110478.
[43] J. Xing, Y. Huang, Q. Xu, et al., ACS Appl. Mater. Interfaces 13 (2021) 28472–28483.
[44] Z. Yang, F. Gao, H. Du, et al., Nano Energy 58 (2019) 768–777.
[45] T. Tunkasiri, G. Rujijanagul, J. Mater. Sci. Lett. 15 (1996) 1767–1769.
[46] G. Xu, G. Shirane, J.R.D. Copley, et al., Phys. Rev. B 69 (2004) 064112.
[47] J.F. Li, S. Wang, et al., J. Am. Ceram. Soc. 83 (2004) 955–957.
[48] T. Karthik, S. Asthana, Mater. Lett. 190 (2017) 273–275.
[49] Z. Li, H. Sun, X. Liu, et al., Ceram. Int. 46 (2020) 11617–11621.
[50] H. Chen, J. Shi, X. Dong, et al., J. Materiom. 8 (2022) 489–497.
[51] H. Qi, A. Xie, J. Fu, et al., Acta Mater. 208 (2021) 116710.
[52] R. Jiménez, M.L. Sanjuán, B. Jiménez, J. Phys.: Condens. Matter 16 (2004) 7493–7510.
[53] G. Liu, L. Chen, H. Qi, Microstructures 3 (2023) 2023009.
[54] Y. Gao, W. Qiao, X. Lou, et al., Adv. Mater. 36 (2024) e2310559.
[55] S. Lan, Z. Luo, Y. Liu, et al., Appl. Phys. Lett. 124 (2024) 090501.
[56] K. Wei, J. Duan, G. Li, et al., J. Alloy. Compd. 994 (2024) 174710.
[57] L. Yang, X. Kong, F. Li, et al., Prog. Mater. Sci. 102 (2019) 72–108.
[58] A. Young, G. Hilmas, S.C. Zhang, et al., J. Am. Ceram. Soc. 90 (2007) 1504–1510.
[59] F. Yan, H. Bai, G. Ge, et al., Small 18 (2022) e2106515.
[60] C. Long, W. Zhou, H. Song, et al., Acta. Mater. 256 (2023) 119135.
[61] H. Ji, D. Wang, W. Bao, et al., Energy Storage Mater. 38 (2021) 113–120.
[62] H. Qi, A. Xie, A. Tian, R. Zuo, Adv. Energy Mater. 10 (2019) 1903338.
[63] D. Hu, Z. Pan, X. Tan, et al., Chem. Eng. J. 409 (2021) 127375.
[64] J. Ye, G. Wang, M. Zhou, et al., J. Mater. Chem. C 7 (2019) 5639–5645.
[65] L. Liu, Y. Liu, J. Hao, et al., Nano Energy 109 (2023) 108275.
[66] F. Yan, Y. Shi, X. Zhou, et al., Chem. Eng. J. 417 (2021) 127945.
[67] L. Zhang, R. Jing, Y. Huang, et al., J. Materiom. 8 (2022) 527–536.
[68] X. Dong, X. Li, X. Chen, et al., J. Materiom. 7 (2021) 629–639.